



# Consistent Quantification of Precipitate Shapes and Sizes in Two and Three Dimensions Using Central Moments

Felix Schleifer<sup>1</sup> · Moritz Müller<sup>1</sup> · Yueh-Yu Lin<sup>1</sup> · Markus Holzinger<sup>1</sup> · Uwe Glatzel<sup>1</sup> · Michael Fleck<sup>1</sup>

Received: 23 December 2021 / Accepted: 15 March 2022 / Published online: 11 April 2022  
© The Author(s) 2022

## Abstract

Computational microstructure design aims to fully exploit the precipitate strengthening potential of an alloy system. The development of accurate models to describe the temporal evolution of precipitate shapes and sizes is of great technological relevance. The experimental investigation of the precipitate microstructure is mostly based on two-dimensional micrographic images. Quantitative modeling of the temporal evolution of these microstructures needs to be discussed in three-dimensional simulation setups. To consistently bridge the gap between 2D images and 3D simulation data, we employ the method of central moments. Based on this, the aspect ratio of plate-like particles is consistently defined in two and three dimensions. The accuracy and interoperability of the method is demonstrated through representative 2D and 3D pixel-based sample data containing particles with a predefined aspect ratio. The applicability of the presented approach in integrated computational materials engineering (ICME) is demonstrated by the example of  $\gamma''$  microstructure coarsening in Ni-based superalloys at 730 °C. For the first time,  $\gamma''$  precipitate shape information from experimental 2D images and 3D phase-field simulation data is directly compared. This coarsening data indicates deviations from the classical ripening behavior and reveals periods of increased precipitate coagulation.

**Keywords** Shape quantification · Data analysis technique · Image processing · Microstructure analysis · Precipitate size

## Introduction

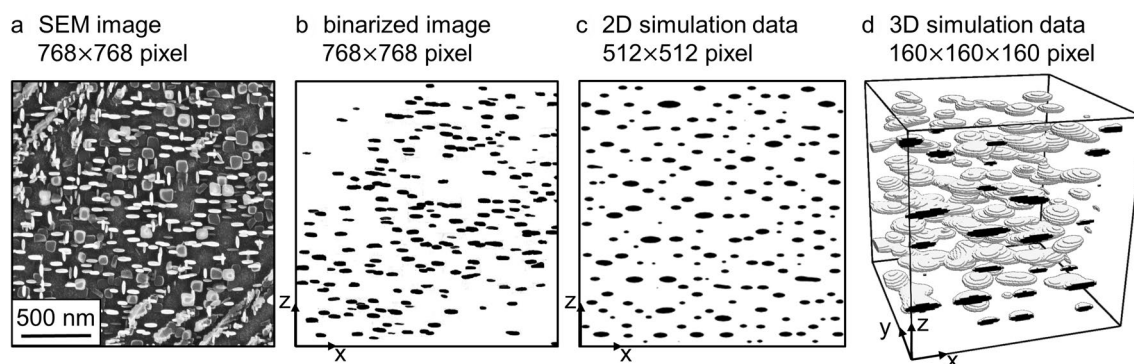
Accurate modeling of materials thermal processing plays an essential role in the field of integrated computational materials engineering (ICME). Computational methods allow optimization of the alloy processing towards full exploitation of the strengthening potential of precipitation of ordered phases. Computational microstructure design focuses on precipitate sizes and size-distributions and on precipitate shapes. In this work, we present an approach for consistent quantitative microstructure description that is consistently valid for heterogeneous types of microstructure data representation.

Figure 1 gives an overview over types of data representation that ICME methods must be able to handle. Figure 1a

shows a scanning electron microscopy (SEM) image of the  $\gamma''$  precipitate microstructure in a Ni-based alloy cropped to a size of  $768 \times 768$  pixels [1]. The matrix phase is etched so the plate-like precipitates are fully visible as elongated shapes in the image. Figure 1b shows a binarized image with a white matrix and black precipitates. Only one specific orientation variant of  $\gamma''$  is shown. This work will not focus on the binarization of the experimental images but on the further processing of the binary data. For binarization, segmentation by a neural network has proven to be a very promising approach [2, 3]. Figure 1c and d show snapshots from two-dimensional (2D) and three-dimensional (3D) phase-field simulations of the microstructure. All numerical discretization schemes are based on simple cubic lattices, and thus, the numerical grid points are referred to as pixels. In Fig. 1b, c and d, the crystallographic tetragonal direction  $\vec{c}$  of the depicted precipitates is parallel to the  $z$ -axis. In Fig. 1a, the sample is oriented such that the tetragonal direction of a precipitate is either in the image plane parallel to the  $x$  axis or  $z$ -axis, or normal to the image plane.

✉ Michael Fleck  
michael.fleck@uni-bayreuth.de

<sup>1</sup> Metals and Alloys, University of Bayreuth,  
Prof.-Rüdiger-Bormannstraße 1, 95447 Bayreuth, Germany



**Fig. 1** **a** SEM image of plate-like  $\gamma''$  precipitates in alloy 718 M, **b** binarized image of a single orientation variant of  $\gamma''$  and **c** 2D Phase-field simulation **d** 3D phase-field simulation. **a–c** are taken from a previous contribution [1]

The 2D simulation data in Fig. 1c resembles the binarized SEM image of Fig. 1b in many ways. However, 2D models fail to consider the extent of the precipitates in the third dimension. This third dimension is crucial for microstructure description as it distinguishes between needle- and plate-like precipitates. Plate- or needle-like precipitates are observed when the matrix phase exhibits cubic symmetry, and the precipitate phase exhibits tetragonal symmetry [4, 5]. Tetragonal symmetry contains one Cartesian direction, the tetragonal direction  $\vec{c}$ , that is different from cubic symmetry. Needle shapes are more extended in this direction than in the other two, while plates are compressed in this direction. The tetragonal direction is normal to the precipitates habit-plane [4]. The formation of plate-like or needle-like precipitate shapes depends on the anisotropy of the lattice misfit [6]. Exemplary systems of industrial relevance that exhibit plate-like tetragonal precipitates in a cubic matrix phase are Al–Cu alloys with the  $\theta'$  precipitates [7, 8],  $\text{ZrO}_2$  ceramics [9] and Ni–Fe–Nb alloys with  $\gamma''$  precipitates [10]. The elastic state in 2D simulations is assumed to be plane-strain (assuming infinitely extended precipitates) which imposes a limitation to 2D simulation of the precipitate microstructure. To fully describe the complex mechanisms of microstructure formation at this length-scale a 3D simulation setup is required. To obtain experimental 3D images of many precipitates with sizes of a few hundred nanometers is very challenging. The precipitates are too small and show too little contrast for computer tomography analysis. Nano-resolved methods like atom probe tomography are limited to sample volumes that can include a few whole precipitates at most. Therefore, the experimental tool-set to observe the precipitate microstructure consists mainly of scanning (SEM) or transmission electron microscopy (TEM).

Quantification of the precipitate shape provides important insight into relevant modeling parameters such as the interfacial energy [9, 11–13], lattice misfit [14, 15], diffusivity [16], precipitate strengthening potential [17] and the degree of morphological degeneration [18]. The shape of plate-like

precipitates is commonly described by the ratio between the plate's diameter and its thickness, the aspect ratio. Precipitate aspect ratios are evaluated from darkfield TEM images by manually measuring the minimum and maximum extents of individual precipitates [19–22]. 3D simulation data of plate-like particles can be evaluated by slicing through the precipitate, fitting a circle to the resulting shape and measuring the extent normal to the slice [23]. This method is effective yet requires a-priori knowledge about the precipitate orientation. Another approach to comparing 3D simulations to the 2D experimental images is to take individual 2D slices from the simulation domain [1]. In this case, information about the 3D shape of the precipitates is lost. Ideally, the slices are chosen such that all individual precipitates are cut exactly once to ensure the statistical accuracy of the data. Slicing without any depth information cannot yield reliable precipitate sizes as the cuts are rarely through the particle barycenter.

The sub-grain microstructure of Ni-based superalloys contributes significantly to the mechanical properties of the material. During heat treatment of alloy 718, plate-like  $\gamma''$  (Ni<sub>3</sub>Nb) precipitates are formed with a major radius or plate radius  $R_M$  smaller than 200 nm. Some authors report the radius of a sphere with equal volume  $R_E$  to quantify the precipitate size independently of the precipitate shape [24]. The precipitate shape is usually assumed to be an oblate spheroid, i.e., a uniaxially compressed sphere [5]. Elastic interactions between neighboring precipitates at high volume fractions were found to cause deviations from this shape towards faceted shapes with increased aspect ratio [12] and increased in-plane edginess [1]. The precipitate size is controlled by aging heat treatments [25]. During service at high temperatures, the  $\gamma''$  microstructure coarsens significantly, meaning that the mean precipitate size increases. This microstructure coarsening ultimately limits the lifetime of aerospace and stationary gas turbine components [26]. An example of modern microstructure design is the deliberate precipitation of  $\gamma''$  on the edges of cubical  $\gamma'$  precipitates to

enable the production on large superalloy parts [27]. An in-depth understanding of the factors that influence the coarsening kinetics of the plate-like  $\gamma''$  precipitates is key to the successful application of ICME methods to improve lifetime and to optimize the thermal processing conditions.

The second-order central moments have proven to be a useful basis for microstructural description [28, 29]. 2D phase-field simulation data on  $\gamma''$  precipitate coarsening has successfully been analyzed by the method of moment invariants [30]. The shape of cuboidal  $\gamma'$  precipitates and the in-plane shapes of  $\gamma''$  shapes have been analyzed in 2D simulations and experimental images by the moment invariants [1, 11]. For the quantification of the formation of a raft-like microstructure from cuboidal precipitates the method of moment invariants was applied to 2D and 3D data [18]. The second-order central moments can also be used to quantitatively compare 2D and 3D data of the grain structure [31, 32]. Until now, there is no unified approach for aspect ratio quantification for plate-like precipitates that is equally valid in two and three dimensions.

In this work, we present a stable, efficient and easy to implement way to quantify the shapes of arbitrary plate-like particles. The approach works consistently in two and three dimensions and is applicable to experimental and simulation data alike. No a-priori knowledge about particle orientation in 3D is required. In Section “Shape Quantification by Central Moments”, we will describe the method of central moments and its application to particle shape quantification. In Section “Performance Analysis”, the performance of the approach is tested on arbitrarily generated 2D and 3D shapes. In Section “Application of the Method in an ICME Context”, the potential of the approach is demonstrated on etched and oriented experimental 2D microstructure images and a 3D simulation of  $\gamma''$  precipitate coarsening in a Ni-based superalloy at 730 °C.

## Shape Quantification by Central Moments

All considered particles are compact bodies with different lateral extents in all Cartesian directions. As a general plate-like particle we define a tri-axial ellipsoid given by

$$\left(\frac{x}{r_3}\right)^2 + \left(\frac{y}{r_2}\right)^2 + \left(\frac{z}{r_1}\right)^2 \leq 1 \quad (1)$$

with the half-axes  $r_1, r_2, r_3$ . The plate-like particle is now defined in the Cartesian coordinates  $x, y, z$  with the tetragonal direction  $\vec{c}$  parallel to  $z$ . Cuts through the particle barycenter parallel to the main planes and projections of the particle shape to the main planes render three ellipses with well-defined aspect ratios. Given  $r_1 < r_2 \leq r_3$  we define three aspect ratios  $A = r_2/r_1, B = r_2/r_3$  and  $C = r_3/r_1$  with  $A \geq C \geq B \geq 1$ . Two

of the aspect ratios are independent and  $C = A/B$ . The largest aspect ratio of any 2D cut through the particle is  $A$  and  $B$  is the smallest.  $B$  can also be understood as the aspect ratio of a top view on a plate. In the case of tetragonal symmetry, we find  $B = 1$ .

Figure 2 shows the tri-axial ellipsoid with three different radii. Cuts normal to  $r_1$  (green),  $r_2$  (blue) and normal to  $r_3$  (red) are indicated together with the aspect ratio of the resulting 2D shapes  $B, C$  and  $A$ , respectively. The projections of the particle shape to image planes parallel to the cuts render the same shapes as the cuts due to the convex shape of the particle.

## Aspect Ratio Quantification from Central Moments

The moments  $\mu_{klm}$  are defined as the integral over the particle  $V$  [33]

$$\mu_{klm} = \int_V x^k y^l z^m dV, \quad (2)$$

with the Cartesian coordinates  $x, y, z$ . The integer exponents  $k, l, m \geq 0$  determine the order of the moment as  $(k + l + m)$ . The zero-order moment  $\mu_{000}$  is equal to the volume of the particle and the first-order moments indicate the barycenter of each particle. We define the central moments  $\bar{\mu}_{klm}$  as

$$\bar{\mu}_{klm} = \int_V \bar{x}^k \bar{y}^l \bar{z}^m dV, \quad (3)$$

where  $\bar{x}, \bar{y}, \bar{z}$  are the coordinates relative to the barycenter of the particle and thus  $\bar{\mu}_{100} = \bar{\mu}_{010} = \bar{\mu}_{001} = 0$ . On a pixel grid, the integrals Eqs. (2) and (3) reduce to sums. It shall be noted here, that the approach is not limited to simple cubic finite-difference discretization but works with arbitrary spatial discretization.

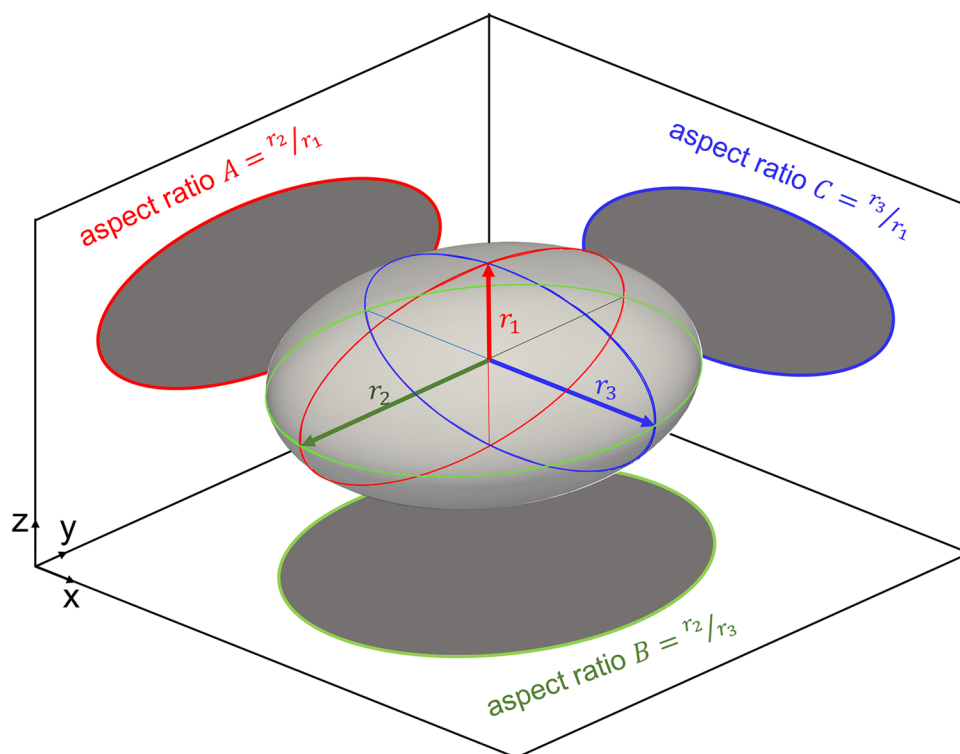
We define the aspect ratios of arbitrary particles as the aspect ratios of a tri-axial ellipsoid that has equal principal central moments. We define the inertia matrix  $\Lambda$  from the second-order central moments as

$$\Lambda = \begin{bmatrix} \bar{\mu}_{020} + \bar{\mu}_{002} & -\bar{\mu}_{110} & -\bar{\mu}_{101} \\ -\bar{\mu}_{110} & \bar{\mu}_{200} + \bar{\mu}_{002} & -\bar{\mu}_{011} \\ -\bar{\mu}_{101} & -\bar{\mu}_{011} & \bar{\mu}_{200} + \bar{\mu}_{020} \end{bmatrix}, \quad (4)$$

with eigenvalues  $\lambda_1 \leq \lambda_2 \leq \lambda_3$ . The eigenvalues of the second-order central moments are invariant to rotation and translation. The aspect ratios of a best-fitting tri-axial ellipsoid can be calculated via [34]

$$A = \sqrt{\frac{\lambda_2 + \lambda_3 - \lambda_1}{\lambda_1 + \lambda_2 - \lambda_3}}, B = \sqrt{\frac{\lambda_2 + \lambda_3 - \lambda_1}{\lambda_1 + \lambda_3 - \lambda_2}}. \quad (5)$$

**Fig. 2** Cuts through a tri-axial ellipsoid with half-axes  $r_1, r_2, r_3$  and projections to planes parallel to the cuts. The aspect ratios of the cuts and projections are  $A = r_2/r_1$ ,  $B = r_2/r_3$  and  $C = r_3/r_1$



In 2D there are two non-zero eigenvalues as  $\lambda_1 = 0$ . The aspect ratio of an ellipse that represents the particle shape in moment space is then given as [35]

$$A = \sqrt{\frac{\lambda_3}{\lambda_2}}. \quad (6)$$

To further describe the precipitate shape, affine invariants can be calculated from the second-order central moments, that are invariant under scaling and stretching operations [11, 18, 28, 29].

### The Plate Shape of $\gamma''$ Precipitates

A stringent comparison between 2D experimental images and 3D ripening simulation data requires a consistent measure for precipitate sizes. This is especially important when non-spherical precipitate shapes are considered, and preferential growth directions exist. To compare 2D and 3D representations of the  $\gamma/\gamma''$  microstructures in terms of the precipitate shapes, we introduce a generalized plate aspect ratio  $A_p = \sqrt{AC} = \sqrt{A^2/B}$  (see Fig. 2). In 2D we assume that  $A = C$  (and thus  $A_p = A$ ) as we have no information about how far the precipitate extends outside of the image plane. This assumption is reasonable for tetragonal precipitates with the tetragonal direction in the image plane.  $A_p$  is the geometric mean of the maximum and minimum aspect ratio of a projection of a

precipitate that rotates around the tetragonal direction to a plane that includes the tetragonal direction. This value is the expected mean when statistically many precipitates are cut. The aspect ratio  $A_p$  is the three-dimensional generalization of the aspect ratio of an equivalent ellipse that was proposed for the analysis of 2D simulation data [30]. To measure the aspect ratio variation in a single precipitate, we introduce the orthogonality of the shape  $\omega = A - A_p$ . This value is 0 for tetragonal symmetry of the shape ( $B = 1$ ) and greater than 0 for  $B > 1$ . The parameter  $\omega$  indicates how much the aspect ratio varies when the precipitate is rotated around the tetragonal direction.

Figure 3a and b visualize the plate aspect ratio  $A_p$  of a 3D precipitate at the example of a tri-axial ellipsoid with  $A = r_3/r_1 = 2.4$  and  $B = r_3/r_2 = 1.4$ . The plate aspect ratio is  $A_p = 2.0$  with  $\omega = 0.4$ . The precipitate shape is now approximated by an ellipsoid with tetragonal symmetry  $A = A_p$  and  $B = 1$  that has the same volume as the precipitate. The deviation of the aspect ratio  $A_p$  from the aspect ratio  $A$  is  $\omega$ .

Figure 3c shows how an etched sample of  $\gamma''$  precipitates embedded in a matrix phase and the SEM image relate. Etching removes matrix from the surface of the sample to fully reveal the precipitate. When the sample is oriented such, that the tetragonal direction  $\vec{c}$  lies inside the image plane, the visible projection of the precipitate shape corresponds to the cuts through the precipitate that are depicted in Fig. 3a and b.



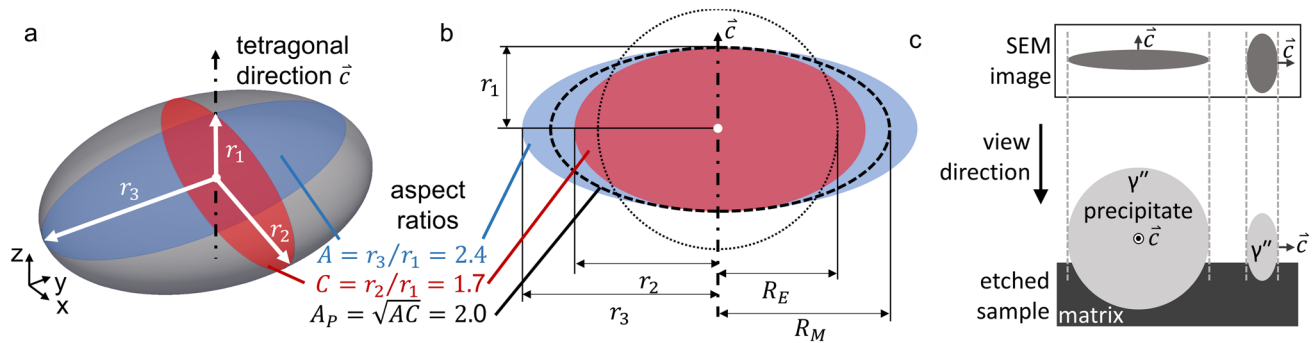


**Fig. 3** **a** Tri-axial ellipsoid with cuts through its barycenter with minimum and maximum aspect ratios. **b** Both cuts together with the measures for precipitate size  $R_M$  and  $R_E$ . **c** Relation between the ori-

ented and etched sample and the SEM image. The precipitate shapes are projected to the image plane and are fully visible

We can now calculate the major radius of the precipitates  $R_M$  consistently in 2D and 3D only from the moments  $\bar{\mu}_{klm}$  calculated via Eq. (3) in 2D as

$$R_M = \left( \frac{\mu_{000}}{\pi} A_P \right)^{1/2}, \quad (7)$$

and in 3D as

$$R_M = \left( \frac{3\mu_{000}}{4\pi} A_P \right)^{1/3}. \quad (8)$$

Note that this formulation makes  $R_M$  independent of the orthogonality  $\omega$ . The length is dimensionless and must be scaled with the magnification of the underlying images or the length scaling of the simulation accordingly (nm per pixel).

Another measure of the size of a precipitate is the radius of a sphere with equal volume to the precipitates  $R_E$  [24]. This measure is independent of preferential growth directions and can be calculated by

$$R_E = R_M \cdot (A_P)^{-1/3}. \quad (9)$$

Figure 3b shows the precipitate size and aspect ratio measures all together. The minimum extent is the radius  $r_1$  in tetragonal direction. The minimum and maximum radius of 2D projections of the shape that include  $r_1$  are  $r_2$  and  $r_3$ , respectively (see also Fig. 2a). The major radius of the plate-like precipitate is then the radius of an ellipsoid with  $B = 1$  and  $A = A_P$ . We now have a consistent set of variables that describe the precipitates in terms of their size  $R_M$  and  $R_E$ , aspect ratio  $A_P$ , and deviation from tetragonal symmetry  $\omega$ . All parameters can be consistently derived from plate-like precipitates in 2D and 3D microstructures. Both definitions of the precipitate size,  $R_M$  and  $R_E$ , require quantification of the precipitate's aspect ratio and the area or volume of the

precipitate. To correctly extract both the size and the aspect ratio of the precipitates from an SEM image, the precipitates must be oriented with their tetragonal direction in the image plane. The matrix phase must be etched to fully reveal the precipitates.

## Performance Analysis

### Generation of Arbitrarily Plate-Like Particles

To quantify the precision of the presented approach to analyze the aspect ratios of particles, sets of 2D and 3D particles with defined shapes are generated. The binary image is generated from a projection of 3D shapes to a pixel grid. The shapes consist of a cylinder with height  $h$  and an elliptical base area with radii (half-axes)  $w/2 \geq b/2$ . The cylinder is topped on both face planes with half a tri-axial ellipsoid with the same base area as the cylinder and a third radius  $(d - h)/2$ . The shape has a total thickness of  $d$ . The shape is then classified by the aspect ratios  $w/d$ ,  $w/b$  and by a shape parameter  $S = h/d$ .  $S$  is 0 for purely ellipsoidal shapes and 1 for purely cylindrical shapes. A similar parameter is used for shape classification of cuboidal precipitates [28]. The corresponding 2D shapes are generated from a rectangle  $w \times h$  and two half ellipses with radii  $w/2 \geq (d - h)/2$ . The binary image is generated by projecting the shapes to a pixel grid with a binary encoding. When half or more of the pixel lies inside the shape, it is assigned the value 1 (black) and 0 (white) if less than half of it is outside the shape, respectively.

Figure 4a and b show a side and top view of a shape defined by the parameters  $w/d = 2.5$ ,  $w/b = 1.5$  and  $S = 0.4$ . Figure 4c shows the 2D shape that is derived by projection to the pixel grid. The particle area is 355 pixels. Figure 4d shows the consistently derived 3D shape with a volume of 5500 pixels. The binary particles have an imposed

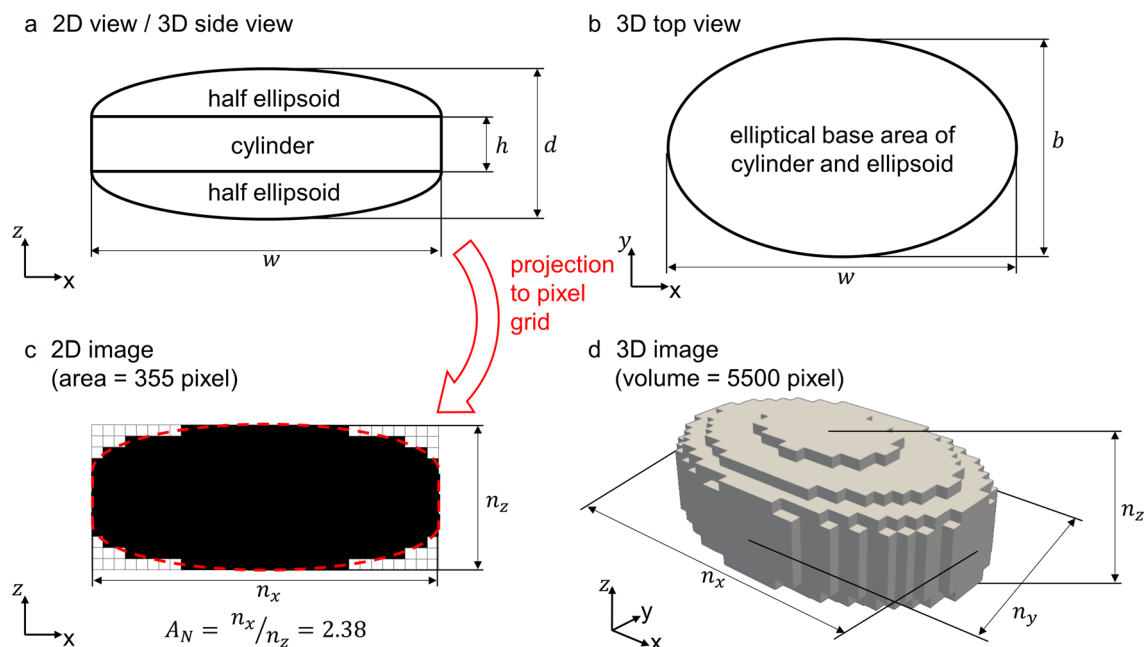


**Fig. 4** Schematic for 2D and 3D particle image generation. **a** 2D view or side view in 3D with  $w/d = 2.5$  and shape parameter  $S = h/d = 0.4$ , **b** top view with  $w/b = 1.5$ , **c** derived binary 2D image of particle with imposed aspect ratio  $A_N = 2.38$  and **d** derived 3D particle with  $B_N = 1.48$

aspect ratio  $A_N$  that is defined as  $A_N = n_x/n_z$  with  $n_x$  the maximum extent of the particle in  $x$ -direction and  $n_z$  in  $z$ -direction. The imposed aspect ratio  $B_N = n_x/n_y$  is defined accordingly. In Fig. 4c and d the imposed aspect ratio is  $A_N = 31 \text{ pixels} / 13 \text{ pixels} = 2.38$  and in Fig. 4d  $B_N = 1.48$ . The deviations from  $w/d = 2.5$  and  $w/b = 1.5$  are due to the coarsely chosen resolution of the pixel grid.

### Accuracy of Aspect Ratio Quantification

The accuracy of the method of central moments for quantification of aspect ratios is tested on sets of 2D particles resolved by 5000 pixels and by 370 pixels, respectively. The lower resolution corresponds to the resolution of the precipitates in Fig. 1b and c. 3D particles are resolved by 5500 pixels. This resolution corresponds to the low 2D resolution as it provides a comparable extent of the particle in a single direction. The exact number of pixels per particle varies slightly between different shapes due to the binary data representation. The particles are generated according to the schematic in Fig. 4 with  $w/d$  varied between 1.2 and 7.4 and  $w/b$  varied between 1.0 and 1.5. Therefore, the overall shape of the particles is still considered a plate rather than a needle ( $B \ll A$ ). The shape factor  $S$  is varied between 0 (purely ellipsoidal) and 1 (purely cylindrical). All generated shapes are normalized to the same area or volume.

Figure 5 shows the aspect ratio calculated from the moments plotted against the imposed aspect ratio of the binary representation of the particles. Figure 5a and b show

the results for 2D particles resolved by 5000 and 370 pixels. The shape parameter  $S$  is color coded. The maximum relative deviation between the measured aspect ratios is 3% in both cases. The precision is in the same range as the deviations between the ideal particle shape and the imposed aspect ratio after binarization. The relative error  $F_N$  that arises from uncertainty of the particle boundary position by a single pixel in 2D can be approximated by

$$F_N = \frac{1}{n_x} \approx \frac{1}{\sqrt{NA}}, \quad (10)$$

where  $N$  is the number of pixels that the particle is resolved with and  $A$  is the particle aspect ratio. A small change in the major radius of an elliptical particle will lead to the inclusion of another pixel and thus to an increased aspect ratio. In case of a particle with an aspect ratio of 2.5 resolved by 370 pixels we find  $F_N \approx 3\%$ . This explains the deviation between  $w/d$  and  $A_n$  in Fig. 4. The accuracy of the aspect ratio quantification by this means increases with image resolution and aspect ratio. The method thus provides accurate aspect ratios with a precision in the same range as the overall inaccuracy of the image binarization.

In Fig. 5c, results are given for 3D particles resolved by 5500 pixels. The measurement of the aspect ratio is accurate in a sense that the trend is very well depicted. With deviations higher than in the 2D case (maximum deviation of 19%) the precision of the measurement is lower than in two dimensions. With increasing shape factor  $S$  the obtained

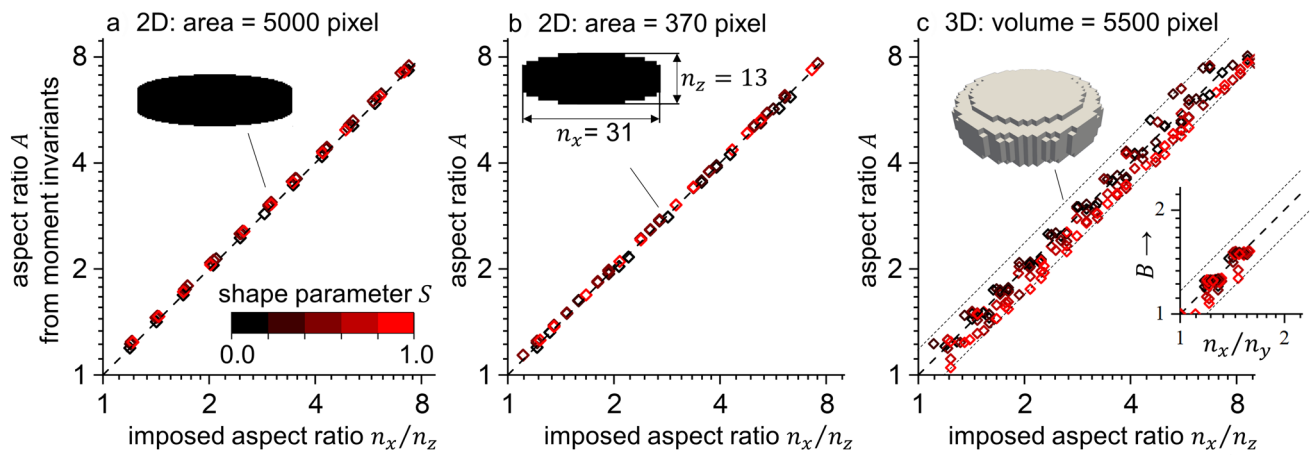


**Fig. 5** Accuracy of the aspect ratio quantification by central moments. Aspect ratios calculated from the moments are plotted as a function of the imposed aspect ratio  $n_x/n_z$ . The shape parameter  $S$

is color coded. **a** 2D particles resolved by 5000 pixels. **b** 2D particles resolved by 370 pixels. **c** Aspect ratios  $A$  and  $B$  of 3D particles resolved by 5500 pixels

aspect ratio drops relative to the imposed ratio. In Fig. 5c, a magnification of the aspect ratio  $B$  plotted over  $n_x/n_y$  is given. The precision of  $B$  is comparable to the precision of  $A$  with a maximum deviation of 16%. The precision for purely elliptical particles with shape parameter  $S = 0$  is considerably better with a maximum deviation of 11% for  $A$  and 7% for  $B$ .

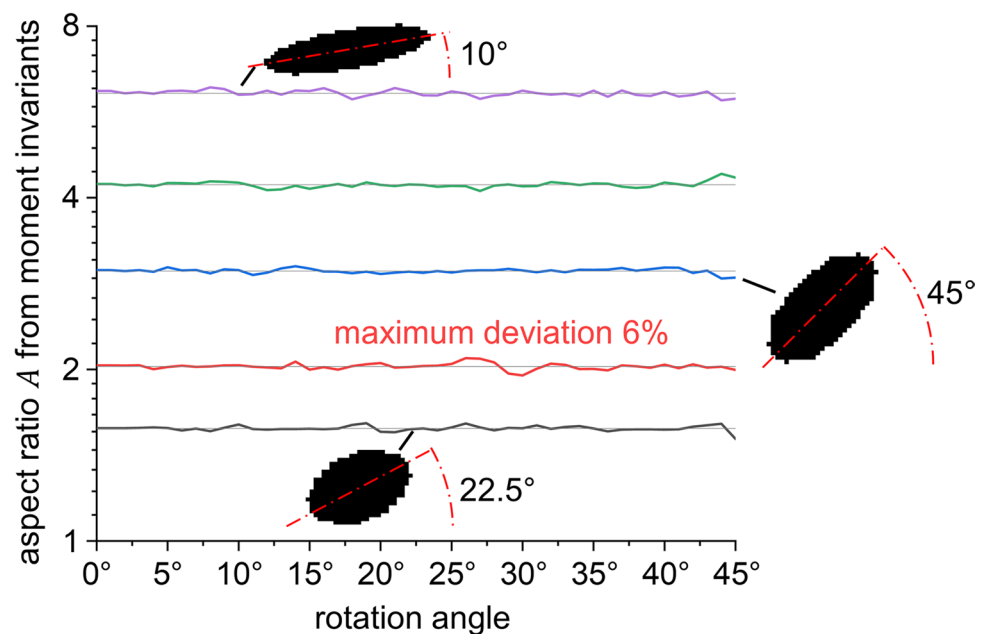
### Rotational Invariance of the Proposed Approach

The imposed aspect ratio that is evaluated by pixel-wise counting of the particle extents can only yield correct aspect ratios when the orientation of the particle relative to the

pixel grid is a-priori known. In contrast to that, the quantification of the aspect ratio by central moments works independently of the particle orientation relative to the pixel grid. To test this, the generated shapes shown in Fig. 4a are rotated around their barycenter before being projected to the pixel grid.

Figure 6 shows the measured aspect ratio  $A$  of five elliptical 2D particles (shape parameter  $S = 0$ ) as a function of the angle by which they were rotated before binarization. The particles are resolved by 370 pixels and a maximum of  $45^\circ$  of rotation is considered due to symmetry. The maximum relative deviation is 6% between maximum and minimum

**Fig. 6** Measured aspect ratio  $A$  of elliptical 2D particles as measured by the moments as a function of the angle by which they are rotated before binarization. Particles are resolved by 370 pixels



aspect ratios and 4% between the maximum and the imposed aspect ratio at zero rotation relative to the pixel grid.

Figure 7a shows an exemplary 3D particle (taken from a microstructure simulation) that strongly deviates from the ellipsoid introduced in Fig. 2. The particle is partially concave and exhibits no symmetries. For the considered particle the imposed aspect ratios are  $A_N = 5.2$  and  $B_N = 2.8$  and the aspect ratios calculated from the moments are  $A = 8.0$  and  $B = 2.5$ . Fig. 7b shows 2D projections of the particle shapes with overlaid ellipses. The ellipses indicate the aspect ratios calculated by the moments. The enveloping box indicates the imposed aspect ratios.

From Fig. 7, it becomes evident that, even though the particle shape significantly differs from the tri-axial ellipsoid from which the presented approach is derived, the measured aspect ratios represent the observed shape. This is another advantage of the rotational invariance of the aspect ratios  $A$  and  $B$  and is beneficial for statistical microstructure analysis.

## Application of the Method in an ICME Context

### Coarsening of $\gamma''$ Precipitates in Ni-Based Superalloys

Plate-like  $\gamma''$  precipitates show inhibited growth kinetics in tetragonal direction due to the anisotropic lattice misfit strain and thus form oblate ellipsoids [5]. The precipitates are classified by their size and their aspect ratio which can both be extracted from 2D images in which the precipitates are fully visible and correctly oriented. The shape of a precipitate is a function of the ratio between its interfacial energy and

elastic bulk energy and thus a function of the precipitate size [36].

During long-term exposure to elevated temperatures the microstructure coarsens, i.e., the mean precipitate size increases. The underlying mechanism is Ostwald-ripening, where large precipitates grow on behalf of smaller ones via bulk diffusion [37, 38]. The change in the mean precipitate size  $\langle R_L \rangle$  over the time  $t$  during Ostwald-ripening is usually assumed to follow

$$\langle R_L(t) \rangle^3 - \langle R_L(0) \rangle^3 = K_L \cdot t \quad (11)$$

where  $R_L(0)$  is the precipitate size at  $t = 0$  and  $K_L$  is the ripening constant with unit  $\text{m}^3 \text{s}^{-1}$ . The index  $L \in [\text{M}, \text{E}]$  in  $K_L$  indicates that the ripening constant is depending on the definition of the precipitate size  $L$ . The brackets indicate the arithmetic mean. Definitions of the two measures for precipitate size, the precipitate major radius  $R_M$  and the equivalent radius  $R_E$  of a sphere with equal volume as the precipitate, are given in Fig. 3. The latter definition does not consider the preferential growth of the precipitates, and therefore, the ripening coefficient  $K_E$  in Eq. (11) can be understood as a measure of diffusive volume transport over time. Compared to spherical precipitates, plate-like precipitates show accelerated ripening kinetics and needle-like precipitates show sluggish coarsening kinetics due to the curvature of the interface [39]. The ripening coefficient is assumed to depend linearly on the precipitate aspect ratio [40]. This effect shows again why a 3D simulation set up is required for quantitative description of the microstructure formation. In 2D set ups a distinction between plates and needles is not possible.

At realistic precipitate volume fractions, growth of precipitates leads to coalescence of neighboring precipitates [1]. This effect leads to an increase in the observed coarsening

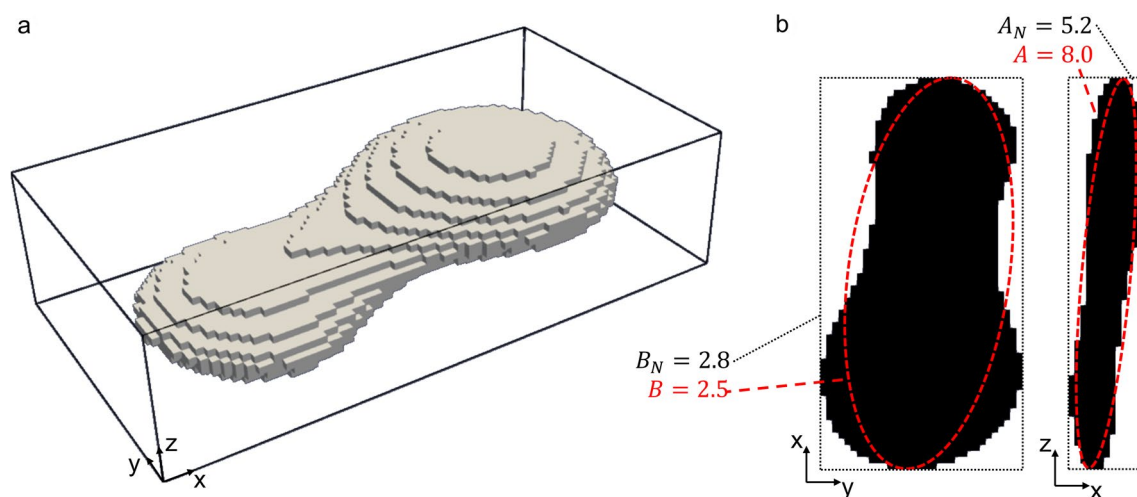


**Fig. 7** **a** 3D shape from microstructure simulation. **b** 2D projection of the particle shape with ellipses indicating the calculated aspect ratios  $A$  and  $B$  and box indicating the imposed aspect ratios  $A_N$  and  $B_N$



kinetics [19]. Figure 8 shows the two coarsening mechanisms that lead to an increase in the mean precipitate size. Figure 8a–c shows precipitate Ostwald-ripening. Smaller precipitates dissolve over the time and large precipitates grow on their behalf. Figure 8d–f visualizes precipitate coalescence where two neighboring precipitates merge during their growth. A concave transient precipitate shape is formed (Fig. 8e), which quickly tends towards the equilibrium precipitate shape again. Both mechanisms can be observed when the system is at equilibrium phase fraction [1].

### Microstructural Analysis of $\gamma''$ Precipitates in Experiment and Simulation

Experiments were carried out with the alloy Ni–Cr18–Fe16–Nb5–Mo3 (in wt%), a derivative of alloy 718, which only includes the cubic matrix phase and the tetragonal  $\gamma''$  precipitate phase [41, 42]. The material was cast as a single-crystal in a proprietary Bridgman investment casting furnace (built by chair of Metals and Alloys, University of Bayreuth, Germany) with a spiral grain selector [1] and was subsequently homogenized for 24 h at 1150 °C followed by water quenching. This treatment effectively dissolves Nb segregations and avoids precipitation of other phases [41]. After the solution heat-treatment, the samples were aged at 730 °C for 6 h or 10 h to study the coarsening. After 6 h of aging the equilibrium volume content of  $\gamma''$  is reached. The coarsening observed during the following 4 h of aging is due to ripening and coalescence [43] as depicted in Fig. 8.

Samples for scanning electron microscopy (SEM) were prepared and the matrix phase was electrolytically etched with phosphoric acid solution (3%  $\text{H}_3\text{PO}_4$ ) at 5 V.

Microstructure images were taken with a SEM 1540EsB (Zeiss, Germany) with a column-near secondary electron detector (Z-contrast). To ensure applicability of the method of central moments the samples are oriented with one crystallographic  $\langle 001 \rangle$ -direction of the single crystal parallel to the electron beam. Together with the removed matrix this yields 2D projections of the precipitates with their tetragonal direction  $\vec{c}$  either in the image plane or normal to it. At this point we assume that the projection of the precipitate is equal to a cut through its barycenter parallel to the image plane as depicted in Fig. 3c.

The SEM images were binarized for each orientation variant of the precipitates separately (see Fig. 1a, b). From the two variants that are oriented with their tetragonal direction in the image plane, and thus appear elongated, the central moments were calculated. The edge length of a pixel is 2.5 nm for images taken after 6 h and 5.0 nm for images taken after 10 h of aging. The original data has been published by the authors in a previous contribution [1]. Precipitates that touch the boundary of the image and are thus not fully visible are excluded from the analysis.

The simulation of  $\gamma''$  ripening was conducted using a sharp phase-field model that uses a field  $\varphi(\vec{x}) \in [0, 1]$  to distinguish between the cubic matrix phase and the  $\gamma''$  precipitates [44, 45]. Values of  $\varphi$  between 0 and 1 indicate a phase boundary. The model considers diffusion of Nb [43, 46], elastic strain due to the lattice misfit and interfacial energy [12]. The thermodynamic and mechanic input data needed for the simulation is taken in accordance with previous work by the authors [1, 12]. The interfacial energy density of 175 mJ m<sup>-2</sup> was found to best reproduce experimental precipitate shapes [12]. The diffusivity of Nb is  $2.5 \cdot 10^{-17} \text{ m}^2 \text{ s}^{-1}$  [47].

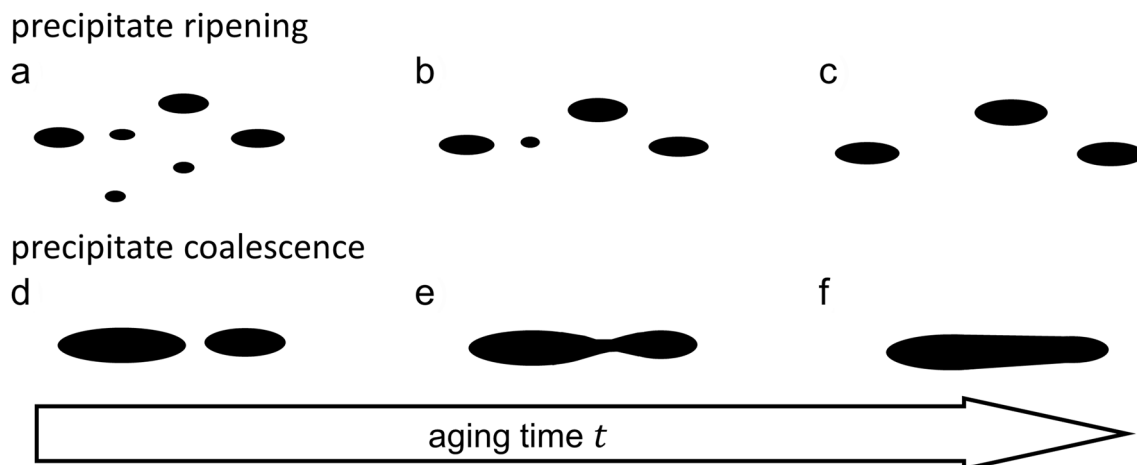


**Fig. 8** Coarsening mechanisms of plate-like precipitates at equilibrium phase fraction. **a–c** smaller precipitates dissolve due to Ostwald ripening and large precipitates grow. **d–f** Coalescence of two growing precipitates under formation of a transient concave precipitate shape (**e**)

The simulation was carried out on a grid of  $160^3$  pixels. The edge length of the pixels corresponds to a physical length of 1.9 nm. The domain boundaries are subject to periodic boundary conditions. An initial microstructure that represents the experimentally observed microstructure after 6 h of aging heat-treatment is generated by randomly distributing 400 precipitates with a volume of  $1000 \pm 100$  pixels and an aspect ratio of 3. This corresponds to a volume fraction of 10% which is in good agreement to the experimentally observed volume fraction [48, 49]. The local concentration of Nb is initialized as the phase-wise equilibrium composition. The volume of the precipitates is randomly varied, and the precipitates are distributed such that there is no overlap between individual precipitates. 4 h of precipitate ripening were simulated. The 3D microstructure is binarized before calculation of the moments such that any pixel with  $\varphi \geq 0.5$  is considered precipitate phase and all the others are matrix. This ensures comparability between the data representation in 2D and 3D. Due to the periodic boundaries, all precipitates that touch the domain walls are included in the analysis.

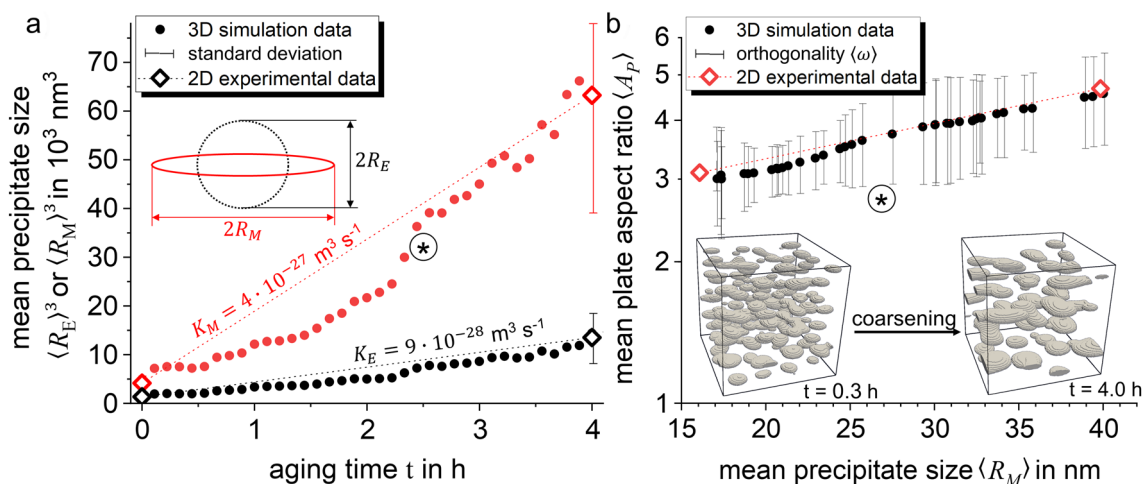
### Kinetics of $\gamma''$ Precipitate Coarsening During Aging

Figure 9a shows the mean precipitate size  $\langle R_M \rangle$  and  $\langle R_E \rangle$  raised to the third power and plotted over the aging time (starting after 6 h of initial aging heat-treatment). The experimental data points are connected by a dotted line that indicates the expected coarsening behavior after Eq. (11). The slopes of these lines are the coefficients of ripening  $K_M = 4 \cdot 10^{-27} \text{ nm}^3 \text{ s}^{-1}$  and  $K_E = 9 \cdot 10^{-28} \text{ nm}^3 \text{ s}^{-1}$ . The simulated precipitate size evolution differs from the linear trend that is assumed. The simulated curves of  $\langle R_M \rangle^3$  and  $\langle R_E \rangle^3$  over  $t$  are bent upwards, which indicates ripening with

an exponent smaller than the exponent of 3 in Eq. (11). This trend is significantly more pronounced for the major radius  $R_M$  than for the equivalent radius  $R_E$ .

Figure 9b shows the size-dependence of the precipitate aspect ratio. The mean plate aspect ratio  $\langle A_p \rangle$  is plotted over the mean precipitate major radius  $\langle R_M \rangle$ . Error bars of  $\pm \langle \omega \rangle$  are added that show how much the aspect ratio of the 3D precipitates varies. Two exemplary simulation domains after 0.3 h and 4.0 h of coarsening are also depicted. From the initial 400 simulated precipitates 75 were left after 4 h of simulated ripening. The simulation can accurately predict the size-dependence of the precipitate shape that is experimentally observed. The deviation from tetragonal symmetry, depicted by the error bars, drops after 0.5 h due to an initial phase of precipitate coalescence. Precipitates that were initialized close to each other merged shortly after simulation start and then diffusively changed their shape towards their equilibrium shape (see Fig. 8b). After around 2.5 h, another period of enhanced precipitate coalescence can be observed in both Fig. 9a as a steep increase in mean precipitate size and in Fig. 9b as an increase in  $\langle \omega \rangle$ . This is indicated by the asterisk (\*).

The size-dependence of the precipitate aspect ratios is the reason for the upwards bent curves in Fig. 9a. The precipitates show preferential growth in two directions, leading to an increasing aspect ratio and therefore to increased ripening coefficients [39, 40]. The continuously accelerated ripening leads to the observed deviation from classical ripening behavior. The preferential growth alone explains the deviation of the major radius  $\langle R_M \rangle^3$  from the proposed linear behavior. The nonlinear course of the equivalent radius  $\langle R_E \rangle^3$ , that is defined independently of the precipitate shape,



**Fig. 9** Comparison between data of precipitate coarsening at 730 °C from experimental 2D images and 3D simulation data. **a** Temporal development of the precipitate major radius  $R_M$  and equivalent radius

$R_E$  during aging at 730 °C. **b** Size-dependence of the mean plate aspect ratio with two exemplary 3D data sets. The asterisk (\*) indicates increased precipitate coalescence

demonstrates the effect of the continuously accelerated ripening kinetics.

By application of the proposed method for aspect ratio quantification, it is possible to distinguish between two very intricate effects that influence  $\gamma''$  coarsening kinetics. By measuring the deviation from tetragonal symmetry of the precipitate shapes, we can identify periods of increased precipitate coalescence rates. By using the precipitate shape to measure the equivalent radius  $R_E$  we can observe how the shape evolution of growing precipitates leads to deviations from classical ripening kinetics.

## Conclusion

We present an approach to quantify the shape and size of precipitate particles based on their central moments. The approach is consistently applicable to two-dimensional images and three-dimensional simulation data. Thus, it allows to consistently compare precipitate shapes and sizes from experimental two-dimensional images with those from three-dimensional microstructure simulation results. The method is particularly helpful to deal with the challenging case of plate-like particles, as it provides a generic definition of the aspect ratio of arbitrarily shaped particles. The aspect ratio is defined based on unique properties in the particles moment space that are tailored to converge to the correct aspect ratio values in case of an ellipsoid. The high accuracy of the method and its applicability in integrated computational materials engineering (ICME) is demonstrated in different scenarios. The following conclusions were met:

- The three-dimensional shape of any plate-like particle is described by two aspect ratios derived from the second-order central moments. The plate radius is determined from the geometric mean of the two aspect ratios and the precipitate volume. The other measure of the precipitate is the radius of a sphere with equal volume.
- Even at low resolutions, the determination of the aspect ratios of arbitrary particles is highly accurate: The aspect ratio of a 2D shape resolved by only 370 pixels is measured with a precision of 97%. The aspect ratios of a similar 3D shape are measured with equally high accuracy and with a precision of 81%.
- The calculated aspect ratios are independent from the particle orientation relative to the pixel grid. At the lowest tested resolution of 370 pixels, rotation of the particle relative to the pixel grid leads to a maximum deviation of the aspect ratio of 4%.
- The accurate quantification of a statistically relevant number of precipitate shapes and sizes provides insights into the intricate contributions to the coarsening kinetics

of  $\gamma''$  precipitates. The observed microstructure coarsening deviates from the classical model of Ostwald ripening. By measuring the radius of a sphere with equal volume as the precipitate, it is possible to show that this is an effect of the size-dependent aspect ratio of the  $\gamma''$  precipitates. The deviations from the expected tetragonal symmetry of the precipitates reveal periods of increased precipitate coalescence.

**Acknowledgements** This work is funded by the Deutsche Forschungsgemeinschaft (DFG) with grant numbers GL181/53-1, FL826/3-1, and FL826/5 and by the Federal Ministry for Economic Affairs and Climate Action (BMWi) under the project SAPHIR (funding code: 03EE5049D).

**Funding** Open Access funding enabled and organized by Projekt DEAL.

**Data Availability** The generated benchmark particle data is available under <https://doi.org/10.5281/zenodo.5801074>.

## Declarations

**Conflict of interest** The authors declare no conflict of interest.

**Open Access** This article is licensed under a Creative Commons Attribution 4.0 International License, which permits use, sharing, adaptation, distribution and reproduction in any medium or format, as long as you give appropriate credit to the original author(s) and the source, provide a link to the Creative Commons licence, and indicate if changes were made. The images or other third party material in this article are included in the article's Creative Commons licence, unless indicated otherwise in a credit line to the material. If material is not included in the article's Creative Commons licence and your intended use is not permitted by statutory regulation or exceeds the permitted use, you will need to obtain permission directly from the copyright holder. To view a copy of this licence, visit <http://creativecommons.org/licenses/by/4.0/>.

## References

1. Lin Y-Y, Schleifer F, Holzinger M et al (2021) Quantitative shape-classification of misfitting precipitates during cubic to tetragonal transformations: phase-field simulations and experiments. *Materials* (Basel) 14:1373. <https://doi.org/10.3390/ma14061373>
2. Stan T, Thompson ZT, Voorhees PW (2020) Optimizing convolutional neural networks to perform semantic segmentation on large materials imaging datasets: X-ray tomography and serial sectioning. *Mater Charact* 160:110119. <https://doi.org/10.1016/j.matchar.2020.110119>
3. Ahmed M, Horst OM, Obaied A et al (2021) Automated image analysis for quantification of materials microstructure evolution. *Model Simul Mater Sci Eng* 29:55012. <https://doi.org/10.1088/1361-651X/abfd1a>
4. Wen SH, Kostlan E, Hong M et al (1981) The preferred habit of a tetragonal inclusion in a cubix matrix. *Acta Metall* 29:1247–1254
5. Cozar R, Pineau A (1973) Influence of coherency strains on precipitate shape in a FeNiTa alloy. *Scr Metall* 7:851–854

6. Tordjman A, Wasserblat A, Shneck RZ (2020) Revisit of the shape and orientation of precipitates with tetragonal transformation strains that minimise the elastic energy. *Philos Mag* 100:927–954. <https://doi.org/10.1080/14786435.2019.1708987>
7. Da Costa TJ, Cram DG, Bourgeois L et al (2008) On the strengthening response of aluminum alloys containing shear-resistant plate-shaped precipitates. *Acta Mater* 56:6109–6122. <https://doi.org/10.1016/j.actamat.2008.08.023>
8. Vaithyanathan V, Wolverson C, Chen LQ (2002) Multiscale modeling of precipitate microstructure evolution. *Phys Rev Lett* 88:125503
9. Lanteri V, Mitchell TE, Heuer AH (1986) Morphology of tetragonal precipitates in partially stabilized ZrO<sub>2</sub>. *J Am Ceram Soc* 69:564–569
10. Cozar R, Pineau A (1973) Morphology of  $\gamma'$  and  $\gamma''$  precipitates and thermal stability of Inconel 718 type alloys. *Metall Trans* 4:47–59
11. Holzinger M, Schleifer F, Glatzel U et al (2019) Phase-field modeling of  $\gamma'$ -precipitate shapes in nickel-base superalloys and their classification by moment invariants. *Eur Phys J B*. <https://doi.org/10.1140/epjb/e2019-100256-1>
12. Schleifer F, Holzinger M, Lin Y-Y et al (2020) Phase-field modeling of  $\gamma/\gamma''$  microstructure formation in Ni-based superalloys with high  $\gamma''$  volume fraction. *Intermetallics* 120:106745
13. Devaux A, Nazé L, Molins R et al (2008) Gamma double prime precipitation kinetic in alloy 718. *Mater Sci Eng A* 486:117–122. <https://doi.org/10.1016/j.msea.2007.08.046>
14. Tsukada Y, Takeno S, Karasuyama M et al (2019) Estimation of material parameters based on precipitate shape: efficient identification of low-error region with Gaussian process modeling. *Sci Rep* 9:1–11
15. Haas S, Manzoni AM, Holzinger M et al (2021) Influence of high melting elements on microstructure, tensile strength and creep resistance of the compositionally complex alloy Al10Co25Cr-8Fe15Ni36Ti6. *Mater Chem Phys* 274:125163. <https://doi.org/10.1016/j.matchemphys.2021.125163>
16. Zhang J, Poulsen SO, Gibbs JW et al (2017) Determining material parameters using phase-field simulations and experiments. *Acta Mater* 129:229–238. <https://doi.org/10.1016/j.actamat.2017.02.056>
17. van Sluytman JS, Pollock TM (2012) Optimal precipitate shapes in nickel-base  $\gamma$ - $\gamma'$  alloys. *Acta Mater* 60:1771–1783. <https://doi.org/10.1016/j.actamat.2011.12.008>
18. Nguyen L, Shi R, Wang Y et al (2016) Quantification of rafting of gamma' precipitates in Ni-based superalloys. *Acta Mater* 103:322–333. <https://doi.org/10.1016/j.actamat.2015.09.060>
19. Han Y-F, Deb P, Chaturvedi MC (1982) Coarsening behaviour of  $\gamma''$ - and  $\gamma'$ -particles in Inconel alloy 718. *Metal Sci* 16:555–562
20. Sundararaman M, Mukhopadhyay P, Banerjee S (1992) Some aspects of the precipitation of metastable intermetallic phases in INCONEL 718. *Metall Trans* 23(7):2015–2028
21. He J, Fukuyama S, Yokogawa K (1994)  $\gamma''$  precipitate in inconel 718. *J Mater Sci Technol* 10:293–303
22. Slama C, Servant C, Cizeron G (1997) Aging of the inconel 718 alloy between 500 and 750 °C. *J Mater Res* 12:2298–2316
23. Yenusah CO, Ji Y, Liu Y et al (2021) Three-dimensional phase-field simulation of  $\gamma''$  precipitation kinetics in Inconel 625 during heat treatment. *Comput Mater Sci* 187:110123. <https://doi.org/10.1016/j.commatsci.2020.110123>
24. Ahmadi MR, Rath M, Povoden-Karadeniz E et al (2017) Modeling of precipitation strengthening in Inconel 718 including non-spherical  $\gamma''$  precipitates. *Model Simul Mater Sci Eng* 25:55005. <https://doi.org/10.1088/1361-651X/aa6f54>
25. Nicolăi A, Franchet J-M, Bozzolo N et al (2020) Metallurgical analysis of direct aging effect on tensile and creep properties in inconel 718 forgings. In: *Superalloys 2020*. Springer, Cham, pp 559–569
26. Hardy MC, Detrois M, McDevitt ET et al (2020) Solving recent challenges for wrought Ni-base superalloys. *Metall Mater Trans A* 51:2626–2650. <https://doi.org/10.1007/s11661-020-05773-6>
27. Detor AJ, DiDomizio R, Sharghi-Moshtaghin R et al (2018) Enabling large superalloy parts using compact coprecipitation of  $\gamma'$  and  $\gamma''$ . *Metall Mater Trans A* 49:708–717. <https://doi.org/10.1007/s11661-017-4356-7>
28. MacSleynne JP, Simmons JP, de Graef M (2008) On the use of 2-D moment invariants for the automated classification of particle shapes. *Acta Mater* 56:427–437. <https://doi.org/10.1016/j.actamat.2007.09.039>
29. MacSleynne JP, Simmons JP, de Graef M (2008) On the use of moment invariants for the automated analysis of 3D particle shapes. *Model Simul Mater Sci Eng* 16:45008
30. Zhou N, Lv DC, Zhang HL et al (2014) Computer simulation of phase transformation and plastic deformation in IN718 superalloy: microstructural evolution during precipitation. *Acta Mater* 65:270. <https://doi.org/10.1016/j.actamat.2013.10.069>
31. Callahan PG, Groeber M, de Graef M (2016) Towards a quantitative comparison between experimental and synthetic grain structures. *Acta Mater* 111:242–252. <https://doi.org/10.1016/j.actamat.2016.03.078>
32. Callahan PG, Simmons JP, de Graef M (2013) A quantitative description of the morphological aspects of materials structures suitable for quantitative comparisons of 3D microstructures. *Model Simul Mater Sci Eng* 21:15003. <https://doi.org/10.1088/0965-0393/21/1/015003>
33. Hu M-K (1962) Visual pattern recognition by moment invariants. *IRE Trans Inf Theory* 8:179–187. <https://doi.org/10.1109/TIT.1962.1057692>
34. Karnesky RA, Sudbrack CK, Seidman DN (2007) Best-fit ellipsoids of atom-probe tomographic data to study coalescence of  $\gamma'$  (L12) precipitates in Ni–Al–Cr. *Scr Mater* 57:353–356. <https://doi.org/10.1016/j.scriptamat.2007.04.020>
35. Mulchrone KF, Choudhury KR (2004) Fitting an ellipse to an arbitrary shape: implications for strain analysis. *J Struct Geol* 26:143–153. [https://doi.org/10.1016/S0191-8141\(03\)00093-2](https://doi.org/10.1016/S0191-8141(03)00093-2)
36. Thompson ME, Su CS, Voorhees PW (1994) The equilibrium shape of a misfitting precipitate. *Acta Metall Mater* 42:2107–2122. [https://doi.org/10.1016/0956-7151\(94\)90036-1](https://doi.org/10.1016/0956-7151(94)90036-1)
37. Lifshitz IM, Slyosov VV (1961) The kinetics of precipitation from supersaturated solid solutions. *J Phys Chem Sol* 19:35
38. Voorhees PW (1985) The theory of Ostwald ripening. *J Stat Phys* 38:231. <https://doi.org/10.1007/BF01017860>
39. Kozeschnik E, Svoboda J, Fischer FD (2006) Shape factors in modeling of precipitation. *Mater Sci Eng A* 441:68–72. <https://doi.org/10.1016/j.msea.2006.08.088>
40. Boyd JD, Nicholson RB (1971) The coarsening behaviour of  $\theta''$  and  $\theta'$  precipitates in two Al–Cu alloys. *Acta Metall* 19:1379
41. Lin Y-Y, Schleifer F, Fleck M et al (2020) On the interaction between  $\gamma''$  precipitates and dislocation microstructures in Nb containing single crystal nickel-base alloys. *Mater Charact* 165:110389. <https://doi.org/10.1016/j.matchar.2020.110389>
42. Kusabiraki K, Hayakawa I, Ikeuchi S et al (1994) Morphology of  $\gamma''$  precipitates in Ni–18Cr–16Fe–5Nb–3Mo alloy. *Iron Steel* 80:348–352
43. Schleifer F, Fleck M, Holzinger M et al (2020) Phase-field modeling of  $\gamma'$  and  $\gamma''$  precipitate size evolution during heat treatment of Ni-based superalloys. In: Tin S, Hardy M, Clews J et al (eds) *Superalloys 2020*. Springer International Publishing, Cham, pp 500–508
44. Fleck M, Schleifer F, Glatzel U (2019) Frictionless motion of marginally resolved diffuse interfaces in phase-field modeling. preprint <http://arxiv.org/abs/1910.05180>. Accessed 23 Dec 2021

45. Finel A, Le Bouar Y, Dabas B et al (2018) Sharp phase field method. *Phys Rev Lett* 121:25501. <https://doi.org/10.1103/PhysRevLett.121.025501>
46. Fleck M, Schleifer F, Holzinger M et al (2018) Phase-field modeling of precipitation growth and ripening during industrial heat treatments in Ni-base superalloys. *Metall Mater Trans A* 49:4146–4157. <https://doi.org/10.1007/s11661-018-4746-5>
47. Sohrabi MJ, Mirzadeh H (2020) Revisiting the diffusion of niobium in an As-cast nickel-based superalloy during annealing at elevated temperatures. *Met Mater Int* 26:326–332. <https://doi.org/10.1007/s12540-019-00342-y>
48. Brooks JW, Bridges PJ (1988) Metallurgical stability of INCONEL alloy 718. In: *Superalloys 1988*. TMS, pp 33–42
49. Theska F, Stanojevic A, Oberwinkler B et al (2018) On conventional versus direct ageing of alloy 718. *Acta Mater* 156:116–124. <https://doi.org/10.1016/j.actamat.2018.06.034>